LASER & PHOTONICS REVIEWS

www.lpr-journal.org

Fast 3D Optoacoustic Mesoscopy of Neuromelanin Through Entire Human Midbrain Organoids at Single-Cell Resolution

Ludwig Englert, María Lacalle-Aurioles, Nguyen-Vi Mohamed, Paula Lépine, Meghna Mathur, Vasilis Ntziachristos, Thomas M. Durcan, and Juan Aguirre**

Parkinson's disease is a devastating neurodegenerative disorder characterized by loss of neuromelanin-containing dopaminergic neurons. Novel 3D culture systems like human midbrain-like organoids (hMOs) enable new research avenues for patient-specific therapies, but cannot reach their full potential unless rapid optical imaging of entire organoids is enabled. Currently, hMOs have to undergo tissue clearing processes before imaging to overcome light scattering. Since tissue clearing is a lengthy chemical procedure, large ensemble studies and pharmacological longitudinal studies, which require live cultures, are impossible. To address this obstacle, raster scanning optoacoustic mesoscopy (RSOM) is considered for imaging intact hMOs. RSOM is an optical imaging technique that leverages the optoacoustic effect to overcome the need of tissue clearing. Moreover, by using tomographic principles, large specimens can be imaged within minutes. The results confirm that RSOM can image the neuromelanin distribution in complete hMOs at a single-cell resolution. Whole hMO volumes of standard size can be imaged in 4 min. Comparison with bright-field microscopy and histology confirms the ground truth of the RSOM images. This work opens several research opportunities regarding neuromelanin in hMOs with potential to boost research in Parkinson disease.

1. Introduction

Parkinson's disease (PD) is a common age-related neurodegenerative disorder that affects millions of people worldwide, imposing a severe burden to the health care systems.[1] The loss of neuromelanin-containing dopaminergic neurons and the presence of Lewy bodies positive for aggregated alpha-synuclein are two main histological hallmarks of the disease.[2] Despite numerous studies in different experimental models, the progress in discovering disease-modifying treatments is slow, and the pathogenesis of the disease remains elusive.[3]

A novel state of the art model that holds great potential for studying PD mechanisms in vitro are human midbrain-like organoids (hMOs).[4,5] These 3D cell culture systems, generated from induced pluripotent stem cells (iPSC), mimic key features of the human midbrain.[6–8] Namely, they contain functional dopaminergic neurons and neuromelanin granules that are structurally similar to those found in the human substantia nigra.

PD phenotypes in hMOs are often characterized by examining the cytoarchitecture at different maturation stages in cross-sectional studies, using conventional optical imaging systems. Optical

L. Englert, V. Ntziachristos, J. Aguirre
Institute of Biological and Medical Imaging
Helmholtz Zentrum München
85764 Neuherberg, Germany
E-mail: juan.aguirre@uam.es

L. Englert, V. Ntziachristos, J. Aguirre
Chair of Biological Imaging at the Central Institute for Translational Cancer Research (TranslaTUM)
School of Medicine
Technical University of Munich
81675 Munich, Germany

M. Lacalle-Aurioles, N.-V. Mohamed, P. Lépine, M. Mathur, T. M. Durcan
The Neuro's Early Drug Discovery Unit (EDDU)
Department of Neurology and Neurosurgery
McGill University
3801 University Street, Montreal, Quebec H3A 2B4, Canada
E-mail: thomas.durcan@mcgill.ca

J. Aguirre
Departamento de Tecnología Electrónica y de las Comunicaciones
Universidad Autonoma de Madrid
Madrid, Madrid 28049, Spain

J. Aguirre
Instituto de Investigacion Sanitaria de la Fundacion Jimenez Diaz
Madrid, Madrid 28049, Spain

The ORCID identification number(s) for the author(s) of this article can be found under https://doi.org/10.1002/lpor.202300443

DOI: 10.1002/lpor.202300443

imaging techniques can provide rich insights into cellular dynamics and function of organoids.[9] Standard bright-field microscopy allows imaging of the structure of intact hMOs only at shallow depths (≈100 μm) due to the inherent opacity of biological tissues that result from light scattering. Therefore, sectioning of the hMOs into thin slices (2D histology) or the use of tissue clearing methods (3D histology) prior to imaging is required.[10] These processes are time consuming, which increases the research cost and incompatible with live imaging, which limits the possibility of performing longitudinal studies for drug discovery.

There are several techniques that may circumvent the need of tissue clearance, avoiding its fundamental limitations. These techniques are able to go beyond the shallow penetration depth of standard bright field microscopy (mean free path (MFP) of a photon ≈100 μm[10]) by taking advantages of different physical principles. Confocal microscopy with its background rejecting nature is able to visualize melanin in the epidermal basal layer[11] and could therefore be used to visualize neuromelanin in hMOs. However, the penetration depth of conventional confocal microscopy is limited to 2–3 times of the MFP.[10] Furthermore, its contrast mechanism relies on light reflection, which is suitable for morphological imaging, but does not clearly distinguish between cell types and light absorbing exogenous contrasts. Optical coherence tomography preserves high resolution (few micrometers) at relatively high depths (1–2 mm) by making use of the so-called "coherence gating."[12] However, its contrast mechanism relies on light reflection and therefore has the same limitations as confocal microscopy regarding specificity. In comparison, multiphoton microscopy reaches depths superior to confocal microscopy and has even been applied in brain organoid imaging. Nonetheless, multiphoton microscopy cannot be used to observe entire organoids[13] because it can only visualize up to depths of 200 μm.[14] Pure ultrasound methods can reach high resolution deep in tissue (the depth to resolution ratio of ultrasound is ≈200). However, their contrast mechanism based on sound reflection only allows the visualization of morphological features.[13]

Optoacoustic imaging (OA) offers remarkable advantages over traditional optical imaging methods by breaking through the depth limit for high resolution visualization while preserving the advantages of optical absorption contrast.[15,16] OA works on the basis of the detection of ultrasound waves generated within the sample in response to absorbed pulsed light. Since ultrasound scattering in tissue is orders of magnitude weaker than photon scattering, high resolution capabilities are preserved in deep tissue, without the need for tissue clearing. After mathematical processing of the optoacoustic signals, 3D maps of the absorbed light are obtained. The use of different spectral regions allows the label-free visualization of relevant biomolecules and pigments (melanin, hemoglobin, lipids, water) according to their spectral fingerprint.[17] Melanin and hemoglobin are the most prominent light absorbers in the visible and NIR region. Since hMOs do not contain hemoglobin, highly specific optoacoustic signals can be expected from accumulations of neuromelanin in hMOs.

Regarding resolution, the OA domain termed optoacoustic mesoscopy is very promising for hMO imaging, since it bridges the gap between the microscopy and macroscopy domains achieving resolutions between 4 and 40 μm (axial-lateral) through several millimetres of tissue.[13,18] Such high depth to resolution ratio is generally obtained in the implementation named raster scan optoacoustic mesoscopy (RSOM). RSOM make use of lithium niobate based ultrasound detectors with unique ultrawideband (10–180 MHz) technology that is raster scanned on top of the specimen to be imaged, thereby achieving improved depth to resolution ratios[13] over previous approaches.[16,19,20] Since the characteristic lengths of human cells range from 10 to 100 μm, RSOM can image individual cells in deep tissue.[21] The 3D RSOM images are obtained by applying tomographic principles to the time resolved optoacoustic signals obtained from a 2D raster scan. This leads to short acquisitions times since a 2D scan suffices for a 3Dreconstruction via mathematical inversion. Depending on the lasers' repetition rate and implementation, a field of view covering an entire hMO can be acquired within few minutes. The hypothesis of this study states that, adapting the single cell molecular imaging abilities of RSOM in deep tissue to neuromelanin producing midbrain organoids will enable fast 3D imaging of intact hMOs and thus provide information regarding neuromelanin content and distribution potentially relevant to basic and applied research in PD.

We investigated for the first time the ability of RSOM to image intact hMOs. A previously developed RSOM system has been adapted for such imaging tasks and obtained datasets from 5 mature hMOs. Comparison with bright-field microscopy and histology indicates that RSOM can quantitatively visualize the distribution of neuromelanin at single-cell resolution through the entire hMO in only 4 min.

2. Experimental Section

2.1. Cell Line Information and Ethical Approvals

The use of human induced pluripotent stem cells in this research is approved by the McGill University Health Centre Research Ethics Board (DURCAN_IPSC/2019−5374). The AST23-2KO line was provided and generated by Dr. Tilo Kunath from The University of Edinburgh according to methodology described in Chen et al.[22] This line corresponds to the isogenic corrected version of the PD patient line AST23 carrying the SNCA gene triplication.

2.2. iPSCs Maintenance and Generation of hMOs

iPSCs were thawed, seeded, and passaged according to the standardized quality control workflow for iPSCs[23] and hMOs were generated following the optimized protocol by Mohamed et al.[24] Briefly, 10 000 cells from a single-cell suspension of iPSCs were seeded in an Embryoid Body (EB)-Disk^{948} Formation Device (eNUVIO Inc., Montréal, QC, CA) containing neuronal induction media with ROCK inhibitor (to maximize cell survival). The EB Disk^{948} was centrifuged for 10 min at 1200 rpm to aggregate the cells. After 48 h, the EBs were formed, and the medium was replaced with fresh neuronal induction media without ROCK inhibitor. After 2 days, the medium was replaced with midbrain patterning medium, driving the EBs toward the midbrain fate. EBs were then embedded, 3 days later, in 1.5 mL of Matrigel reduced growth factor and incubated for 24 h in tissue induction medium.

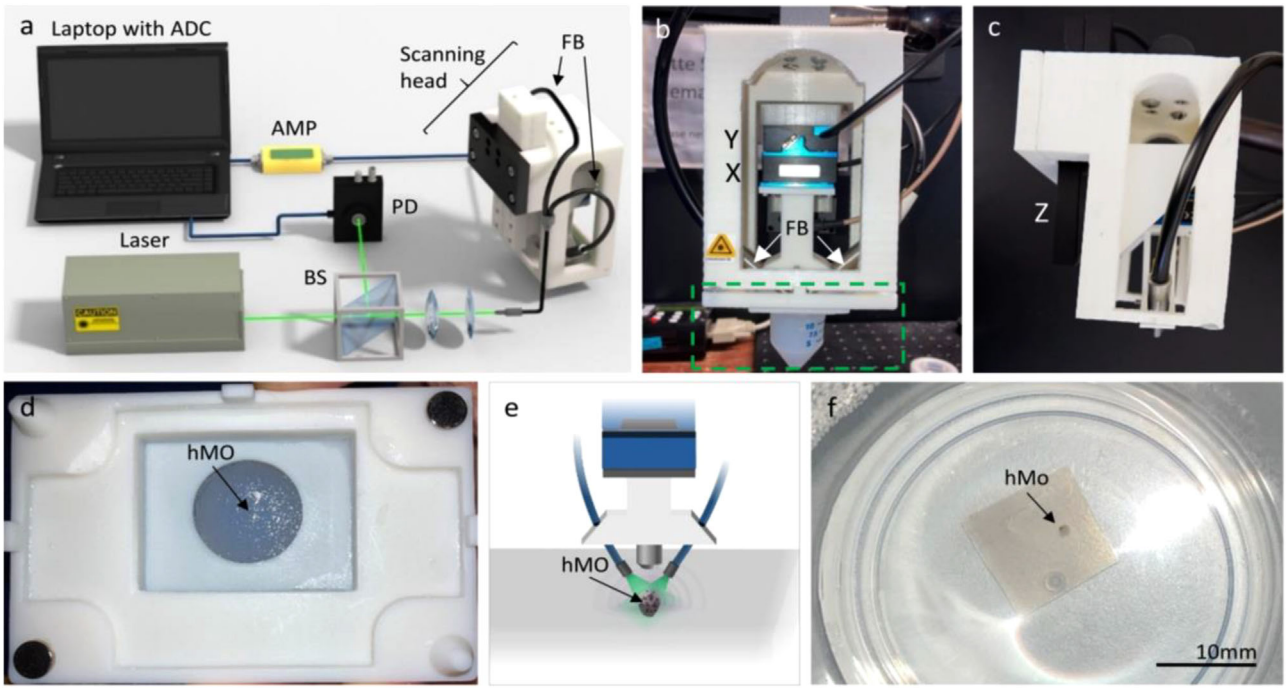

Figure 1. RSOM system adapted to imaging hMOs. a) Schematic of the RSOM system. A laser pulse (532 nm, 2 ns pulse duration) is directed to the sample by optical fiber bundles. Before reaching the fiber bundles (FB) of the scanning head, a part of the beam is diverged to a photodiode (PD), using a beam splitter (BS). The PD triggers the analog-to-digital convertor (ADC). The optoacoustic signals collected by the transducer are amplified (AMP) and sent to the ADC of a laptop. b) Photograph of the front view of the RSOM scanning head. The white arrows indicate the fiber bundles. The transducer is attached to two motorized stages for scanning along the *x*- and *y*-axes (red arrow). The green dashed line indicates the organoid holder, which is also shown in (e). c) Side view of the of RSOM scanning head. The motorized stage responsible for the *z*-axis can be observed. The organoid holder was removed for taking the picture. d) Top view of the organoid holder. The organoid appears as a gray circle in the agar container. The black arrow points to the actual organoid. e) RSOM Scanning principle of the agar embedded organoid. f) hMO embedded in agar cube after RSOM measurement.

Finally, the following day, Matrigel-embedded hMOs were transferred into glass spinner flask (500 mL, Corning, NY) containing 250 mL of final differentiation medium and placed on a magnetic stirrer (Chemglass Life Sciences, Vineland, USA) in an incubator culture set up at 37 °C with 5% CO_2. The medium was replaced once a week and the volume of media was increased up to 500 mL over the maturation phase of hMOs to ensure the quality of the tissue. hMOs were kept in culture for 180 days until spontaneous generation of neuromelanin occurred.

2.3. Tissue Fixation and Preservation

The hMOs were fixed in 4% paraformaldehyde (PFA) for 2 h at room temperature and washed in 1X phosphate-buffered saline (PBS) overnight. On the day after, organoids were transferred to 1X PBS containing 0.02% sodium azide (Sigma-Aldrich, St. Louis, MO), a bacteriostatic preservative, and shipped to the IBMI for RSOM imaging.

2.4. RSOM System, Bright-Field Microscope, and Imaging Protocol

In order to assess RSOM imaging performance, the RSOM images of 5 hMOs with their bright-field microscopy counterparts since the neuromelanin structures appear as brownish/black patterns in the microscopy images were compared. The details of the RSOM system can be found elsewhere in the previous publications.[18,25,26] In brief, the system uses a custom-made spherically focused piezoelectric 50 MHz transducer (BW 10–120 MHz) and 3 mm focal distance (Sonaxis, Besacon, FR). The signals are digitalized with a 1Gs/s 700 MHz data acquisition card (Gagescope RazorMAX, USA). The optoacoustic signals are generated with a 532 nm 1 ns DPSS laser at a pulse rate of 500 Hz (Bright Solutions Wedge HB, IT) (**Figure 1**a). The scan head with the transducer is mounted at the end of an articulated arm. Three motorized stages to allow precise positioning of the transducer in x, y, and z. The stages corresponding to the *x*-axes and *y*-axes allow performance of the RSOM scan (Figure 1b). The *z*-axis is used for placing the transducer at right height with respect to the organoid prior to data acquisition (Figure 1c). The laser light is delivered to the region below the transducer via a custom-made fiber bundle (Ceramoptec, FR). The whole system is controlled with a windows computer via MATLAB.

Upon arrival, each of the 5 selected hMOs were embedded in an agar cube (PBS with 3 % agar, Honeywell-Fluka Analytical, NC), right before reaching the gel point (32–37.5 °C). This allowed to preserve the orientation of the specimens when switching from one imaging modality to another. A special holder was

designed and 3D printed to attach the agar cube firmly to the RSOM scanning head (Figure 1d,e). For each optoacoustic imaging session, the holder is filled with water to ensure acoustic coupling with the transducer (Figure 1f). The ultrasound transducer was scanned over an area of 4 × 3 mm encompassing the entire organoid with a step size of 10 µm. The repetition rate of the laser was set to 500 Hz. With all these parameters, the system needed 4 min to acquire one full data set. The images were reconstructed using the so-called universal backprojection algorithm[27] over a grid of 4 × 2 × 2 mm with a voxel size of 10 × 10 × 3 µm. The lateral resolution of the system is 29.6 µm and the axial resolution is 8.6 µm. The resolution remains constant up to 1.2 mm depth. At the 2.5 mm depth the resolution degrades by 5 µm.[18] The systems resolution is sufficiently high to resolve single neurons which are reported with sizes between 5 µm for the smallest and exceeds 100 µm for the largest neurons in humans.[29] However, neurons below the resolution limit are still detected but appear blurred by the lateral and axial point spread function of the system and therefore still allow the melanin quantification within the organoid. The measured energy per pulse and per area delivered to the sample was 3.60 µJ mm^{-2}, which does not exceed the mean irradiance allowed by the American National Standard for Safe Use of Lasers.

Right after the RSOM imaging session, the agar cubes were removed from the RSOM holder and imaged with an inverted bright-field microscope (Nikon Eclipse TS2-FL). Full organoid images were acquired with a 4 × 0.13 lens objective while a 20 × 0.40 lens objective was used for images with higher magnification to observe the distribution of single neurons.

2.5. Comparison between the RSOM Images and the Bright-Field Microscopy Images

In order to provide a meaningful comparison between the 2D bright-field microscopy images (4 × 0.13 lens objective) and the RSOM 3D reconstructions, the RSOM images were color-coded. A blue colormap for shallow depths (0–300 µm) was used. At those depths, a significant part of the melanin structures falls within the reach of the bright-field images. Common patterns were identified by superimposing the RSOM top view corresponding to the blue colormap with the bright-field images.

A green colormap for the RSOM structures located at depths between 300 and 500 µm was used. Furthermore, a red colormap for depths between 500 and 1000 µm was used. At those depths, the melanin structures would appear significantly blurred on the bright-field images or are simply not displayed. Common patterns in the distribution of neuromelanin were visually identified by superimposing the RSOM top view corresponding to the green or the red colormap with the bright-field images.

To demonstrate the ability of RSOM to resolve the melanin structures at single-cell resolution, 2D bright-field microscopy images were obtained at a higher magnification (20 × 0.40 lens) and the RSOM top view corresponding to the blue colormap (shallow depth). By zooming in the bright-field images, melanin structures distributed in single neurons could be localized. The ability to image single neurons was confirmed by superimposing the corresponding zoom to the RSOM top view.

2.6. Evaluation of the Quantitative Power of the RSOM Data Sets Against Histology

In order to obtain the RSOM quantitative estimation of the amount of neuromelanin, each organoid data set was evaluated based on the voxels of the 3D data set. First, the data was normalized to the highest optoacoustic voxel value along all data sets. Second, a single visually defined threshold (7% for all organoids) was defined to segment the neuromelanin positive voxels (see results) resulting in binary image where the voxels containing melanin have value 1 and the rest 0. For each organoid, the segmentation was controlled visually to ensure that only noisy voxels are rejected. As the current RSOM setup provides contrast only from neuromelanin, no structural reference of the organoid could be used to calculate the ratio of positive voxels along the entire volume of the organoid. Therefore, a 3D cuboid region of interest (ROI) in which the organoids were centred (see results) was selected. The dimensions of the cuboid were kept the same in x- and y-dimensions along all data sets and were also used for the histology to allow a quantitative comparison without segmenting the borders of the organoids. In the z-dimension the box was fitted around the positive voxels individually for each data set. The final percentages of neuromelanin positive voxels for each organoid was calculated as the division of the positive voxels and the total amount of voxels in the 3D ROI.

To have a reference for the RSOM results, the presence of neuromelanin granules using Fontana Masson staining[30] of histological slices in combination with optical microscopy imaging was quantified. hMOs were carefully dissected from the agar blocks and processed for paraffin embedding as follows: hMOs were incubated for 24 h in 70% ethanol, then formalin fixed, dehydrated, and paraffin infused using a tissue processor (HistoCore PEARL by Leica Biosystems, Wetzlar, DE). The hMOs were mounted in paraffin blocks before being sectioned (5 µm thick sections) using a microtome (RM2235, Leica Biosystems). Fontana Masson staining was performed in 2 consecutive sections at 0–200, 200–400, and 400–600 µm deep, using a stain kit (Melanin Stain, #ab150669, Abcam, Cambridge, UK), following the manufacturer's instructions.[8] Full sections were then imaged with the ZEISS Stemi 508 stereomicroscope combined with the ZEISS Axiocam ERc 5 s camera (Zeiss, Jena, DE). Images were acquired with a clinical Olympus BX46 (Olympus, Tokyo, JP) microscope and an Olympus DP27 digital colour camera obtaining Red, Green, and Blue (RGB) images.

The positive pixels for neuromelanin were evaluated by accessing the red channel of the RGB as it offered the best contrast between the neuromelanin and the other structures of the organoid. A single threshold for the slices of all organoids was defined to segment the neuromelanin pixels and visually controlled. Artefacts outside of the organoid were excluded manually, resulting in binary image where pixels with melanin have value 1 and the rest 0. The amount of neuromelanin positive pixels was evaluated in a ROI with the same dimensions as the x- and y-dimensions of the ROI used for the quantitative evaluation of the RSOM data sets. The final percentage of neuromelanin positive pixels was calculated for each organoid as the average of the percentages for each of the slices of the same organoid. In order to compare the RSOM results with histology, linear regression was applied to

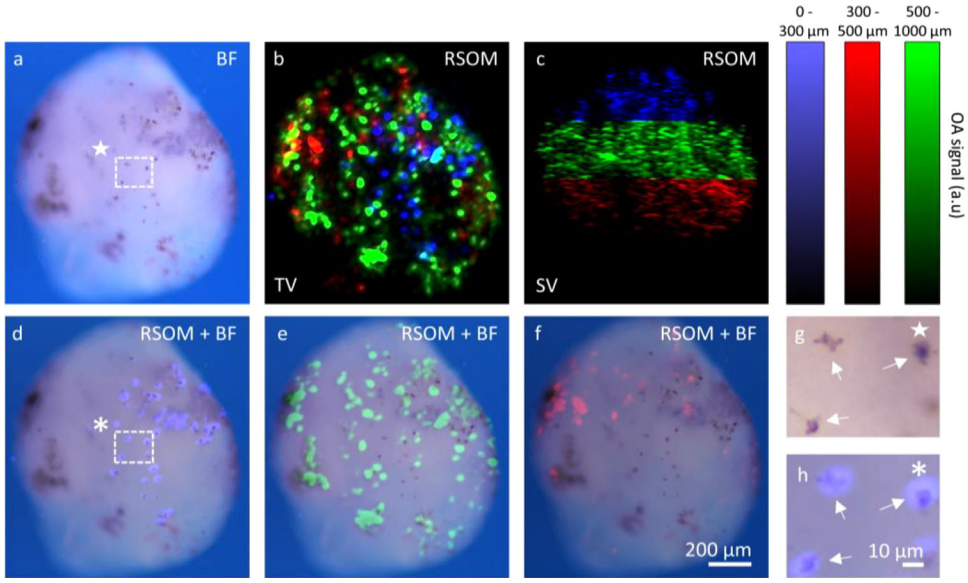

Figure 2. Bright-field microscopy images versus RSOM images of hMO-2. a) Bright-field microscopy image of hMO-2. b) RSOM top view of hMO-2. The organoid is divided in 3 regions according to different depths. For each region one color map applies. The color intensity within each region depends on the optoacoustic signal intensity. c) RSOM side view of d) RSOM top view corresponding to the organoid section ranging from 0 to 300 µm depth overlaid with bright-field image. There is a one-to-one correspondence between the structures shown in RSOM and in bright-field. e) RSOM top view corresponding to the organoid section ranging from 300 to 500 µm depth overlaid with bright-field image with a reasonable correspondence between the structures shown in RSOM and in bright-field. f) RSOM top view corresponding to the organoid section ranging from 500 to 1000 µm depth overlaid with the bright-field image. There is a reasonable correspondence between the structures shown in RSOM and in bright-field. g) Zoomed in region depicted in the bright-field image in a with 3 intracellular melanin structures indicated by 3 white arrows. h) Zoomed in region depicted in the bright field and RSOM overlay in (d) with the same melanin containing structures as in (g) as well as the corresponding RSOM top view in blue. The scale bar in (a–f) corresponds to 200 µm, the scale bar in (g) and (h) corresponds to 10 µm.

examine whether there was a relationship between the RSOM estimate (dependent variable) and histology (independent variable).

2.7. Ethical Statement

The use of human induced pluripotent stem cells (iPSCs) in this research was approved by the McGill University Health Centre Research Ethics Board (DURCAN_IPSC/2019–5374).

3. Results

Figure 1 shows the adapted RSOM system to image hMOs. Figure 1a shows the principle components of the RSOM system including the laser source, beam splitter, photodiode, an analog-to-digital converter, and the motorized scan head. Figure 1b,c shows the scan head from different views with the translational x-,y-, and z-stage, the fiber bundles as well as the customized organoid holder. Figure 1d shows the customized holder in detail with the organoid being embedded in agar. Figure 1e shows the measurement arrangement for performing the scan. Figure 1f shows the agar embedded organoid after the RSOM measurement.

Figure 2 illustrates the capabilities of RSOM to image hMOs using the bright-field microscopy images as a reference. The bright-field microscopy image is shown in Figure 2a. The dark spots correspond to melanin structures, which can be intracellular or extracellular. The deeper structures appear blurred due to light scattering. The top view of the RSOM reconstruction (Figure 2b) shows structures compatible with neuromelanin. The general shape of the organoid according to RSOM follows the shape delineated by the bright-field image. The side view of the RSOM reconstruction illustrates the 3D nature of the optoacoustic images (Figure 2c). Figure 2d–f displays the organoid as a superposition of the bright-field image and the different color-coded layers of the RSOM image. Color-coded top view RSOM cross sections are available as videos (Videos S1–S5, Supporting Information) for all organoids in a "fly-through" mode. The superposition of the superficial RSOM melanin structures with the bright-field ones reveal a high fidelity match (Figure 2d) of the melanin pattern. When comparing the deeper structures (Figure 2e, f) the match is still clear even though the bright-field images are blurred while the RSOM images preserve their resolution. A small misalignment displayed in the overlapping images occur because a perfect match cannot be obtained when overlaying a 3D reconstruction against 2D image constrained by the geometrical effects of the camera model. Moreover, RSOM revealed some melanin structures that are not accessible to bright-field. At higher magnifications in the bright-field images, one can observe intracellular structures of melanin corresponding to a single neuron, which are also depicted by the RSOM system (Figure 2g–i), demonstrating single cell level resolution.

Figure 3 depicts the bright-field microscopy images (Figure 3a–e) and the RSOM top views of hMOs1-5, displaying variable neuromelanin content. 3D RSOM videos for all organoids can be observed in Videos S6–S10 (Supporting

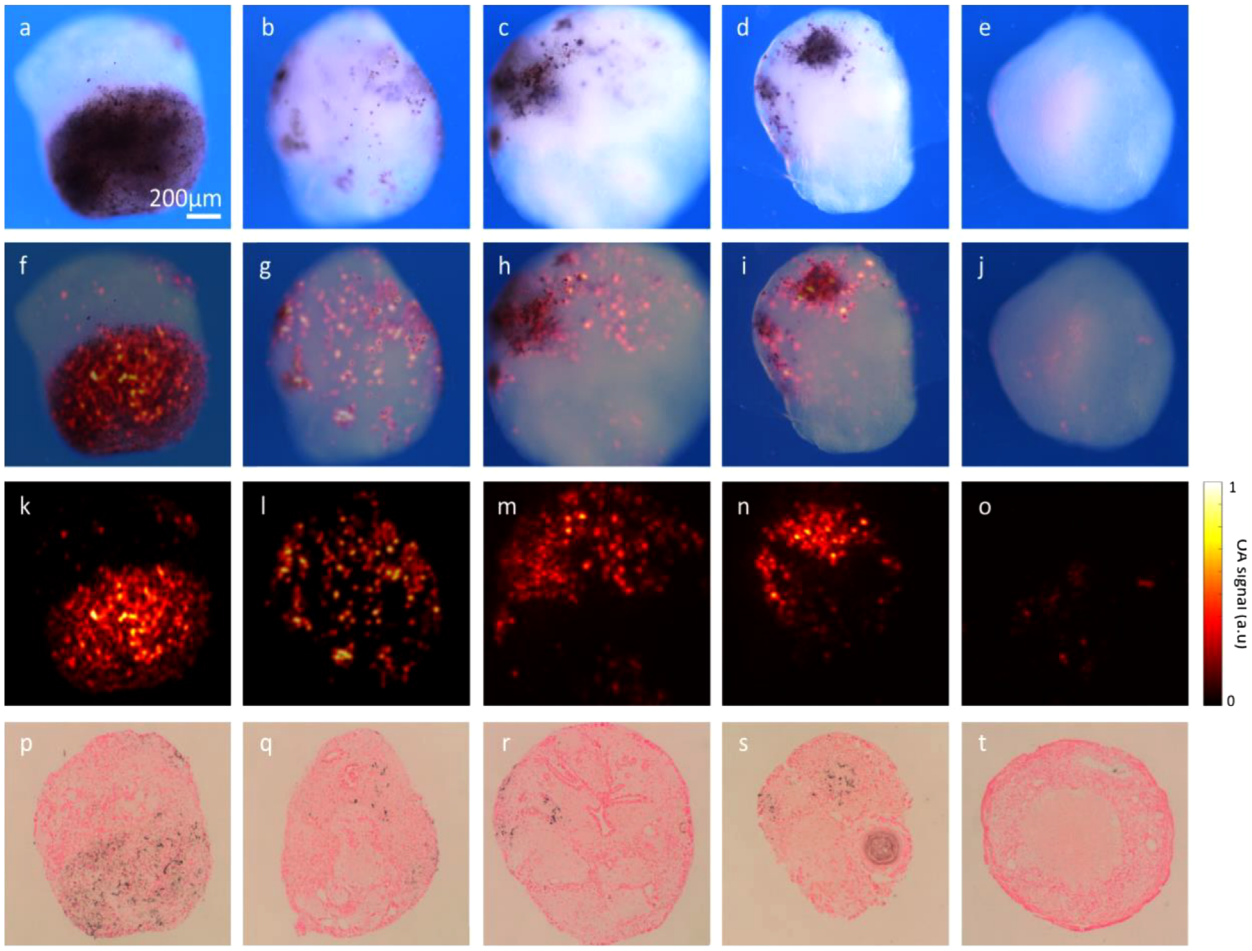

Figure 3. Bright-field microscopy images versus RSOM. a–e) Bright-field microscopy image of hMOs 1-5. f–j) RSOM top view overlaid with the bright-field microscopy image for hMOs 1-5. k–o) RSOM top view of hMOs 1-5. p–t) Fontana Masson-stained slices of hMOs 1-5. The scale bar corresponds to 200 µm.

Information). The graphs corresponding to the superposition of the RSOM top views (full depth) with the bright-field images (Figure 3f–j) show a clear match of the superficial neuromelanin structures. The RSOM top views (Figure 3k–o) reveal deep melanin structures that are not accessible to bright-field system for all hMOs. One out of the six Fontana Masson-stained slices for hMOs 1–5 used for the histology evaluation are shown in Figure 3p–t with melanin appearing in black.

Figure 4 shows the process of quantitative analysis for neuromelanin in RSOM (Figure 4a–c) and the colorimetric analysis of the histology slices for hMO-1. The comparison between the percentages of neuromelanin positive voxels of the RSOM data sets and neuromelanin positive pixels of the colorimetric analysis of the histology for all organoids is shown in Figure 4g. The amount of neuromelanin estimated by RSOM follows a clearly decreasing trend for the 5 organoids. This fits well to the decreasing trend shown in the histology results. Linear regression applied on the results yields a R^2 of 0.895 ($p = 0.0149$), indicating a linear relation between the neuromelanin estimated by RSOM and histology. An error of 7.6–19.8% for hMOs 1–4 (<1% for hMO-5) occurs between the histological and RSOM quantification.

4. Discussion

The results presented in this work indicate that RSOM is effective in imaging the distribution of neuromelanin in entire midbrain organoids noninvasively. RSOM overcomes the hard limitations of classical optical methods concerning imaging depth, imaging time and contrast, thereby opening the possibility for longitudinal studies and large ensemble studies. For the first time, the imaging performance demonstrated in this study has enabled affordable, practical, and quantitative large and/or longitudinal studies of neuromelanin production and distribution. This holds great potential for basic and applied research in PD.

Comparison between RSOM images and the bright-field images for 5 hMOs illustrate the superior imaging capabilities of RSOM for structures well beyond the diffusion limit of conventional microscopy. Several neuromelanin related structures that are not visible using the bright-field microscope can be clearly seen with RSOM. Furthermore, comparison with histological analysis showcased the quantification capabilities of RSOM regarding the distribution of neuromelanin for all organoids. The disagreements between the RSOM estimation of neuromelanin concentration and histology shown in our results (e.g., histology

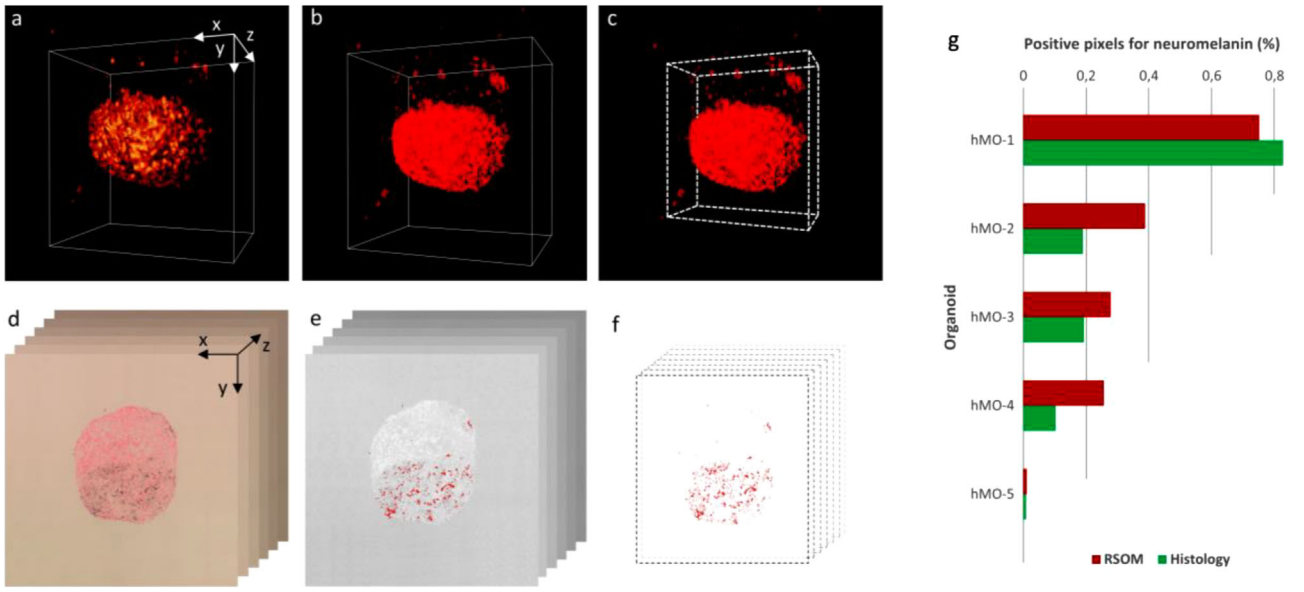

Figure 4. Procedure for RSOM and histological quantification of melanin content and comparison of results. a) RSOM 3D data set with the measurement 3D coordinate system indicated by white arrows. Black voxels represent noise; red/orange voxels represent RSOM signals. b) Thresholded and binarized 3D RSOM data set of hMO-4. Red voxels represent the segmented neuromelanin positive voxels (gray level = 1), black represents nonsegmented void voxels (gray level = 0). c) The 3D ROI used for quantification is depicted with white dashed line encompassing the neuromelanin positive voxels of the dataset. d) Six histology slices of hMO-4 with the corresponding coordinate system indicated by black arrows. e) Red channel of the histology slices of (d) with thresholded and binarized pixels depicted in red. f) 2D ROI indicated by black dashed lines with the same x- and y-dimensions as for the x- and y-dimensions in the RSOM 3D ROI covering the neuromelanin positive pixels of (e). g) Results of the quantitative analysis for neuromelanin positive voxels (RSOM) and pixels (histology) for hMO-1-5.

vs RSOM for hMO-2 and 4 in Figure 4g) may be induced by the rather coarse sampling in the histology, which does not cover all the spatial variations regarding the neuromelanin distribution in a particular organoid. Furthermore, the paraffin embedding of the organoids for the histological analysis leads to a shrinking of the organoid which therefore affects the quantification individually for each of the organoids. Due to the change of the orientation of the organoids during the slicing and Fontana Masson staining process and the volumetric change a 1:1 comparison between structures in the histological slices and the RSOM dataset is not possible. Another source of uncertainty comes with the individual selection of the ROI in the RSOM data sets' z-direction, which may slightly differ from the size of the ROI in the z direction in histology.

The fact that RSOM images show exclusively the neuromelanin distribution of the organoid stems from the optical properties of the different biomolecules in the visible and near infrared region of the electromagnetic spectrum. More specifically, the absorption coefficient of melanin and hemoglobin is several orders of magnitude higher than the one of other bio-compounds. While the melanin signal overlaps with the hemoglobin signal in standard "tissues,"[17] melanin has no possible competitor in the bloodless hMOs. Our previous work[17] indicates that we can expect the melanin signal to be strong and background free in the spectral region extending from 488 to 900 nm.

The deepest imaged point was located ≈700 µm, below the surface, due to the overall diameter of the organoids. In standard tissue, the maximum penetration depth is limited to ≈1.5 mm for green light due to the strong absorption from hemoglobin. However, hMOs do not contain hemoglobin and higher penetrations depths may be achieved at 650 nm. For wavelengths in the NIR, ≈3 mm penetration depth could be achieved without any major loss of contrast and resolution, if the pulse length is preserved (≈2 ns). Further work should evaluate the optimum wavelength selection in order to avoid possible shadowing effects in highly pigmented organoids, including further evaluation and comparison with full fine histology of the entire organoid. Multiple side illumination can also overcome eventual shadowing effects.

Future developments should include the necessary arrangements to allow for live imaging of intact hMOs and to enable longitudinal studies. To this end, imaging holders must be adapted to the characteristic technological constraints of RSOM. The organoid culture media may serve as ultrasonic coupling media and pumping strategies can be designed to keep nutrients and oxygen flowing while keeping the organoids in a fixed position to perform the imaging sessions. Overall, several designs can be easily foreseen. Future work could also include the transition of RSOM to an isotropic axial resolution radially arranged tomographic setup to further overcome the limited lateral resolution. The segmentation of RSOM data may also be improved to allow for an unsupervised threshold selection by adding histogram analysis or machine learning on RSOM data sets. Such implementations could allow to estimate individual segmentation thresholds for each data set. Additional specific contrast in the imaging of live organoids may also be given by transgene molecular tools such as photoswitchable fluorescent proteins adapted for optoacoustic imaging.[28,31]

In summary, in this article we shed light for the first time on the performance of RSOM in imaging hMOs, demonstrating unique imaging capabilities in terms of single cell detection

at high acquisition speed with good quantification abilities for large intact organoids. In its current form, RSOM opens promising research avenues for the neuroscience community working on PD not accessible before. Further technological developments will unlock the full potential of RSOM for the imaging of human brain organoids.

Supporting Information

Supporting Information is available from the Wiley Online Library or from the author.

Acknowledgements

L.E. and M.L.-A. contributed equally to this work. This project was possible thanks to financial support from the Madrid Talento grant 2020-T1/TIC-20661TEC (PRECISION) awarded to J.A. This project has received funding from the European Union's Horizon 2020 research and innovation programme under Grant Agreement No. 687866 (INNODERM) and under Grant Agreement No. 871763 (WINTHER) awarded to V.N. This project has also received funding from Canada First Research Excellence Fund, awarded through the Healthy Brains, Healthy Lives initiative at McGill University, the Sebastian and Ghislaine Van Berkom Foundation and project grant from CIHR (PJT–169095) awarded to T.M.D. Authors would like to thank Ms. Marie-Noëlle Boivin from the C-BIG repository histology core facility at the Neuro for tissue processing and paraffin embedding of the hMOs. Dr. Tilo Kunath generated AST23 lines with funding received from the Medical Research Council, Grant Award No. MR/K017276/1. N.M. is supported by a Fonds de recherche du Québéc-Santé (FRSQ), Parkinson Canada and Parkinson Québéc postdoctoral fellowships. The authors also thanked Dr. Serene Lee for her attentive reading and improvements of the manuscript.

Open access funding enabled and organized by Projekt DEAL.

Conflict of Interest

V.N. is a shareholder in iThera Medical GmbH, a company that commercializes optoacoustic mesoscopy. The company did not provide support for this work.

Data Availability Statement

The data that support the findings of this study are available from the corresponding author upon reasonable request.

Keywords

3D cell cultures, human midbrain organoids, optoacoustics, Parkinson's disease, photoacoustics

Received: May 16, 2023
Published online: July 12, 2023

[1] A. Lee, R. M. Gilbert, *Neurol. Clin.* **2016**, *34*, 955.
[2] W. Poewe, K. Seppi, C. M. Tanner, G. M. Halliday, P. Brundin, J. Volkmann, A.-E. Schrag, A. E. Lang, *Nat. Rev. Dis. Primers* **2017**, *3*, 17013.
[3] E. C. Hirsch, P. Jenner, S. Przedborski, *Mov. Disord.* **2013**, *28*, 24.
[4] N.-V. Mohamed, F. Larroquette, L. K. Beitel, E. A. Fon, T. M. Durcan, *J. Parkinsons Dis.* **2019**, *9*, 265.
[5] S. F. McComish, A. N. MacMahon Copas, M. A. Caldwell, *Front. Neurosci.* **2022**, *16*, 851058.
[6] J. Jo, Y. Xiao, A. X. Sun, E. Cukuroglu, H.-D. Tran, J. Göke, Z. Y. Tan, T. Y. Saw, C.-P. Tan, H. Lokman, Y. Lee, D. Kim, H. S. Ko, S.-O. Kim, J. H. Park, N.-J. Cho, T. M. Hyde, J. E. Kleinman, J. H. Shin, D. R. Weinberger, E. K. Tan, H. S. Je, H.-H. Ng, *Cell Stem Cell* **2016**, *19*, 248.
[7] H. Kim, H. J. Park, H. Choi, Y. Chang, H. Park, J. Shin, J. Kim, C. J. Lengner, Y. K. Lee, J. Kim, *Stem Cell Rep.* **2019**, *12*, 518.
[8] N.-V. Mohamed, J. Sirois, J. Ramamurthy, M. Mathur, P. Lépine, E. Deneault, G. Maussion, M. Nicouleau, C. X.-Q. Chen, N. Abdian, V. Soubannier, E. Cai, H. Nami, R. A. Thomas, D. Wen, M. Tabatabaei, L. K. Beitel, K. Singh Dolt, J. Karamchandani, J. A. Stratton, T. Kunath, E. A. Fon, T. M. Durcan, *Brain Commun.* **2021**, *3*, fcab223.
[9] H.-Y. Tan, H. Cho, L. P. Lee, *Nat. Biomed. Eng.* **2021**, *5*, 11.
[10] V. Ntziachristos, *Nat. Methods* **2010**, *7*, 603.
[11] T. Yamashita, T. Kuwahara, S. González, M. Takahashi, *J. Investig. Dermatol. Symp. Proc.* **2005**, *124*, 235.
[12] A. H. Kashani, C.-L. Chen, J. K. Gahm, F. Zheng, G. M. Richter, P. J. Rosenfeld, Y. Shi, R. K. Wang, *Prog. Retin. Eye Res.* **2017**, *60*, 66.
[13] M. Omar, J. Aguirre, V. Ntziachristos, *Nat. Biomed. Eng.* **2019**, *3*, 354 .
[14] I. Rakotoson, B. Delhomme, P. Djian, A. Deeg, M. Brunstein, C. Seebacher, R. Uhl, C. Ricard, M. Oheim, *Front. Neuroanat.* **2019**, *13*, 77.
[15] A. Taruttis, V. Ntziachristos, *Nat. Photon.* **2015**, *9*, 219.
[16] L. V. Wang, S. Hu, *Science* **2012**, *335*, 1458.
[17] A. Berezhnoi, J. Aguirre, B. Hindelang, N. Garzorz-Stark, M. Omar, U. Darsow, K. Eyerich, V. Ntziachristos, *Opt. Lett.* **2019**, *44*, 4119.
[18] J. Aguirre, M. Schwarz, N. Garzorz, M. Omar, A. Buehler, K. Eyerich, V. Ntziachristos, *Nat. Biomed. Eng.* **2017**, *1*, 0068.
[19] J. Laufer, E. Zhang, G. Raivich, P. Beard, *Appl. Opt.* **2009**, *48*, D299.
[20] C. P. Favazza, O. Jassim, L. A. Cornelius, L. V. Wang, *J. Biomed. Opt.* **2011**, *16*, 16015.
[21] I. Weidenfeld, C. Zakian, P. Duewell, A. Chmyrov, U. Klemm, J. Aguirre, V. Ntziachristos, A. C. Stiel, *Nat. Commun.* **2019**, *10*, 5056.
[22] Y. Chen, K. S. Dolt, M. Kriek, T. Baker, P. Downey, N. J. Drummond, M. A. Canham, A. Natalwala, S. Rosser, T. Kunath, *Eur. J. Neurosci.* **2019**, *49*, 510.
[23] C. X.-Q. Chen, N. Abdian, G. Maussion, R. A. Thomas, I. Demirova, E. Cai, M. Tabatabaei, L. K. Beitel, J. Karamchandani, E. A. Fon, T. M. Durcan, *Methods Protoc.* **2021**, *4*, 50.
[24] N.-V. Mohamed, P. Lépine, M. Lacalle-Aurioles, J. Sirois, M. Mathur, W. Reintsch, L. K. Beitel, E. A. Fon, T. M. Durcan, *Methods* **2022**, *203*, 465.
[25] J. Aguirre, M. Schwarz, D. Soliman, A. Buehler, M. Omar, V. Ntziachristos, *Opt. Lett.* **2014**, *39*, 6297.
[26] B. Andrei, S. Mathias, B. Andreas, O. S. V, A. Juan, N. Vasilis, *J. Biophotonics.* **2018**, *11*, e201700359.
[27] M. Xu, L. V. Wang, *Phys. Rev. E* **2005**, *71*, 16706.
[28] K. Mishra, M. Stankevych, J. P. Fuenzalida-Werner, S. Grassmann, V. Gujrati, Y. Huang, U. Klemm, V. R. Buchholz, V. Ntziachristos, A. C. Stiel, *Sci. Adv.* **2020**, *6*, eaaz6293.
[29] E. Pannese, *Neurocytology: Fine Structure of Neurons, Nerve Processes, and Neuroglial Cells*, Springer International Publishing, Cham **2015**.
[30] P. C. Billings, J. K. Sanzari, A. R. Kennedy, K. A. Cengel, J. T. Seykora, *Exp. Dermatol.* **2015**, *24*, 157.
[31] A. C. Stiel, X. L. Deán-Ben, Y. Jiang, V. Ntziachristos, D. Razansky, G. G. Westmeyer, *Opt. Lett.* **2015**, *40*, 367.